Spectroscopic determination of temperature and density spatial profiles and mix in indirect-drive implosion cores

L. Welser-Sherrill,[1,*] R. C. Mancini,[1] J. A. Koch,[2] N. Izumi,[2] R. Tommasini,[2] S. W. Haan,[2] D. A. Haynes,[3] I. E. Golovkin,[4] J. J. MacFarlane,[4] J. A. Delettrez,[5] F. J. Marshall,[5] S. P. Regan,[5] V. A. Smalyuk,[5] and G. Kyrala[3]

[1]*Department of Physics, University of Nevada, Reno, Nevada 89557, USA*

[2]*Lawrence Livermore National Laboratory, Livermore, California 94550, USA*

[3]*Los Alamos National Laboratory, Los Alamos, New Mexico 87545, USA*

[4]*Prism Computational Sciences, Madison, Wisconsin 53703, USA*

[5]*Laboratory for Laser Energetics, University of Rochester, Rochester, New York 14623, USA*

(Received 16 March 2007; revised manuscript received 25 September 2007; published 16 November 2007)

In the field of inertial confinement fusion (ICF), work has been consistently progressing in the past decade toward a more fundamental understanding of the plasma conditions in ICF implosion cores. The research presented here represents a substantial evolution in the ability to diagnose plasma temperatures and densities, along with characteristics of mixing between fuel and shell materials. Mixing is a vital property to study and quantify, since it can significantly affect implosion quality. We employ a number of new spectroscopic techniques that allow us to probe these important quantities. The first technique developed is an emissivity analysis, which uses the emissivity ratio of the optically thin Lyβ and Heβ lines to spectroscopically extract temperature profiles, followed by the solution of emissivity equations to infer density profiles. The second technique, an intensity analysis, models the radiation transport through the implosion core. The nature of the intensity analysis allows us to use an optically thick line, the Lyα, to extract information on mixing near the core edge. With this work, it is now possible to extract directly from experimental data not only detailed temperature and density maps of the core, but also spatial mixing profiles.

DOI: 10.1103/PhysRevE.76.056403 PACS number(s): 52.57.−z, 52.70.−m

I. INTRODUCTION

Spectroscopy has been used extensively in the field of inertial confinement fusion (ICF) as a powerful nonintrusive diagnostic tool. It provides a method for the characterization of plasma conditions such as temperature and density, which can be extracted in various levels of detail. In addition, we present here a spectroscopic technique which allows the extraction of quantitative information on mixing between material from the shell and the fuel.

Ten years ago, the state-of-the-art technology used to model ICF implosion temperatures and densities was the time-resolved but spatially averaged description of these conditions [1–11]. Essentially, in this approximation the implosion core is treated as a homogeneous object.

It has been suggested, however, that temperature and density spatial profiles are non-negligible in ICF experiments and should be studied [12]. In answer to this, spectroscopic methods evolved with the goal of determining the structure of implosion cores. These techniques focused on interpreting the line spectrum comprising the Ar Heβ and Li-like satellites, along with the associated Heβ narrow-band image [13–15]. More recent advances in diagnostic equipment and analysis methods have made it possible to unfold the spatial information contained in spatially resolved Ar Lyβ and Heβ narrow-band images [16,17].

This work focuses on indirect drive Ar-doped implosions in which Ar Lyβ ($1s-3p$), Ar Heβ ($1s^2-1s3p$), and Ar Lyα ($1s-2p$) narrow-band images were recorded. A variety of objective techniques have been developed to process the narrow-band image data to prepare it for analysis. Using special geometric considerations, it is possible to construct intensity and emissivity maps which can eventually be translated into temperature and density maps of the core, yielding even more detail.

This paper will focus on the determination of temperature and density spatial profiles using several techniques of spectroscopic modeling. The first method, which will be referred to here as the emissivity analysis, enables the extraction of a temperature profile using the emissivity ratio of the Lyβ and Heβ lines. The Lyβ and Heβ equations are then independently solved for the density profiles. The second spectroscopic technique, referred to here as the intensity analysis, involves calculating the density profiles by solving a set of nonlinear discrete transport equations which represent radiation transport through the core. The equations can be solved either in the optically thin approximation or including the effect of opacity. In the latter case, a noticeable change in the density profiles is apparent, particularly in deeper zones of the plasma which have greater optical depth. Hence, we can evaluate the effect of opacity on the core spatial structure determination. The results of these methods are compared to a search and reconstruction technique that uses a genetic algorithm to establish the temperature and density spatial profiles [17,18].

The measurement and investigation of fuel-shell mixing is a topic of great interest in the ICF community [19–21]. Some work has focused on burying tracer elements in the ablator to determine the importance of mixing, a method which cannot yield quantitative mixing trends [22]. Recent work which can

*Present address: Los Alamos National Laboratory, Los Alamos, New Mexico, USA.

identify quantitative mixing information involves the application of particle-based diagnostics [19,20]. In this paper, we discuss the modification of the intensity analysis to include the effects of mixing between the fuel and shell materials. The addition of information from the optically thick Lyα line makes it possible to calculate an extra unknown, the spatial mixing profile. This constitutes an approach designed to directly generate information on mixing from a data analysis, and also an attempt to perform a quantitative analysis of an optically thick image.

II. EXPERIMENTS AND INSTRUMENTS

The indirect drive experiments discussed here were performed at the Laboratory for Laser Energetics' (LLEs) OMEGA laser facility. In each of these experiments, a 2.5 mm long Au hohlraum enclosed a 512 μm-diameter spherical plastic microballoon target filled with 50 atm of D_2 and doped with 0.1 atm of Ar. Thirty OMEGA laser beams, fifteen entering through each laser entrance hole in cones of five and ten beams, were applied in a 1 ns square pulse to irradiate the interior hohlraum walls. This produced a hohlraum radiation temperature of 210 eV, which was sufficient to drive the implosion. Neutron yield was consistently between $3-5\times10^8$ neutrons. An effort was made to use beam pointing which resulted in spherical cores.

The primary diagnostic equipment used was the Multi-Monochromatic X-ray Imager (MMI), which is an innovative instrument designed to record narrow-band images of the core over a wide spectral energy range [16,23]. In this particular case, the MMI records Ar line emission features, which provide the data necessary for spectroscopic diagnosis. MMI also affords the opportunity to subtract continuum images from the line emission images. In addition, space-integrated x-ray line spectra can be extracted from a spatial integration of the image data.

The MMI consists of a pinhole array placed close to the source which acts as the imaging element, and a multilayer mirror Bragg reflector, which provides energy dispersion. The tilt of the rows of pinholes with respect to the spectral dispersion axis leads to each pinhole capturing emission from a small energy range. Figure 1(a) shows clearly the horizontal photon energy axis and the vertically tilted pinhole rows. Integration of several pinhole sub-images is necessary to achieve a full picture of line emission for the Lyβ, Heβ, or Lyα lines [24].

III. DATA PROCESSING TECHNIQUES

This paper focuses on the processing and analysis of MMI data which was time resolved over 50 ps beginning at the time of peak Ar x-ray emission. The MMI captured images in the spectroscopic range of interest, which includes the Lyβ centered at 3935 eV, the Heβ at 3686 eV, and the Lyα at 3320 eV. This range was chosen because attributes of the Lyβ and Heβ lines provide a strong diagnostic sensitivity to both temperature and density [1,13,25]. In addition, the Lyα is an optically thick line which is added in the intensity analysis to provide additional information used to extract mixing profiles.

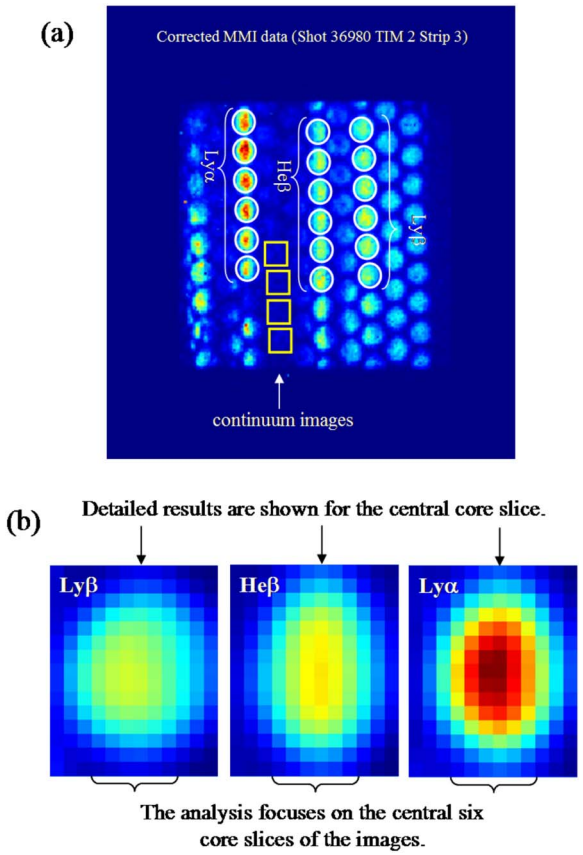

FIG. 1. (Color online) (a) MMI image from indirect drive time-resolved data, corrected for photon energy dependent instrumental effects. Line-based and continuum-based sub-images are highlighted. (b) Final images resulting from the data processing. The columns that are focused on in this paper are indicated.

The MMI data are rich in information, and require a sophisticated tool for image processing. To this end, a graphical user interface was built in IDL to objectively work through the many steps in the processing sequence. Reference [24] provides a detailed explanation of the tool and the procedures. Uncertainties in the image processing procedures are calculated at a 1 to 5% level for the image intensity profiles. In addition, a reliable estimate of the intrinsic uncertainties in the image intensity measurement is ongoing.

Figure 1(a) shows the MMI image after it was corrected for the photon energy dependent instrumental corrections that account for multilayer mirror reflectivity, Be filter transmission, and MCP spectral response. In addition, the data were flat fielded to take into account the variation in response for each pixel. The photon energy axis is depicted, as well as the individual pinhole sub-images that are integrated to compile the Lyβ, Heβ, and Lyα images. Figure 1(b) displays the Lyβ, Heβ, and Lyα images that are generated by aligning the proper sub-images, integrating them, and subtracting the corresponding continuum images. The narrow-band energy ranges are 3875–4015 eV for the Lyβ, 3620–3732 eV for the Heβ, and 3270–3360 eV for the

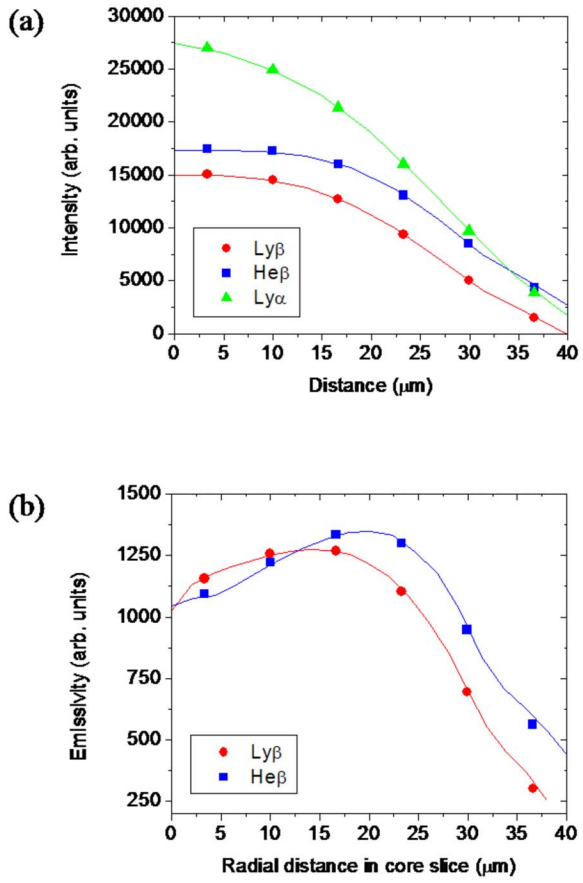

FIG. 2. (Color online) Symmetrized (a) intensity profiles and (b) emissivity profiles from the central core slice, used as input in the spectroscopic analysis.

Lyα. Detailed 1D traces will be presented in this paper for the central column, or core slice, of the images, as indicated in Fig. 1(b). Additionally, spatial maps of temperature and density will be shown for the central six columns.

In the past, angle-integrated radial lineouts of narrow-band images from MMI data were extracted and analyzed [24,25]. This approach connects with the idea of a spherically symmetric core. However, as is noticeable from Fig. 1, these images are not necessarily spherical in nature. A technique has therefore been developed in which a so-called "gummy-worm axis" of the image is identified [26]. This represents a case in which each vertical column of pixels, which corresponds to a core slice of the image, has its own local axis of symmetry.

Each column of an image is symmetrized about this gummy-worm axis, leading to a collection of symmetrized intensity profiles. The symmetrization is used because an inversion based on one line of sight cannot resolve the angular dependence in a core slice. A generalized Abel inversion, in which the intensity of each pixel on the image plane is associated with the line integral of emissivity along a chord in the source, is then performed. Abel inversion can only be used in cases of optically thin line emission [27], which the Lyβ and Heβ lines are often approximated as.

Figure 2 shows the set of symmetrized image intensity profiles and corresponding emissivity profiles for the central core slice of the Lyβ, Heβ, and Lyα images. Note that emissivity profiles are not shown for the Lyα, since it is significantly more optically thick and it is therefore inappropriate to apply an Abel inversion. To provide enough points to characterize trends, the experimental profiles are averaged over six spatial intervals, with some level of partial overlapping. Though this level of detail is finer than the spatial resolution of the MMI data, estimated between 10–12.5 microns, it has been ascertained that the increased resolution in the analysis does not result in significant changes. In this paper, we will focus on the central core slice for the 1D results, and maps of the temperature and density profiles for the central six spatial zones will also be shown, since this part of the image provides the most reliable data for quantitative analysis.

IV. EMISSIVITY ANALYSIS

The first spectroscopic technique discussed here, the emissivity analysis, relies on Lyβ and Heβ data and permits the extraction of both temperature and density spatial profiles. This is accomplished in the optically thin approximation, since the Abel inversion used to generate emissivity profiles assumes an optical depth of zero. In order to reconstruct temperature and density maps of the core, the relationships between emissivity, temperature, and density are exploited. The emissivity of a line transition from an upper level u to a lower level l is proportional to the upper level population number density N_u, the radiative decay rate A_{ul}, the photon energy $h\nu_{ul}$ of the transition, and the area normalized lineshape ϕ_ν,

$$\epsilon_\nu = \frac{1}{4\pi} N_u A_{ul} h \nu_{ul} \phi_\nu. \quad (1)$$

The total line emissivity used in the analysis is a superposition of many single line contributions, including resonance and satellite transitions, in the photon energy range covering a narrow-band image [13]. We emphasize that even though the Heβ and Lyβ line transitions are not themselves significantly affected by opacity, other lines such as the Heα and Lyα are, and their opacity effect does impact the atomic kinetics of the Ar ions [28]. The atomic kinetics model used in the calculation of the emissivities employed in this work does include this opacity effect [13]. The emissivity profiles extracted from the experimental data and shown in Fig. 2 are associated with a column, or core slice, from the original images. The analysis is performed one column at a time, and the columns can then be compiled into maps of the core temperature and density.

The temperature profiles are calculated first by using the idea that the Lyβ/Heβ emissivity ratio is strongly dependent on electron temperature but only weakly dependent on electron density [17]. The analysis uses theoretical emissivities as a function of temperature and density, which are specifically customized for the narrow-band energy range of a particular image, and are generated by the physics model discussed in Ref. [13].

Figure 3 demonstrates the surface resulting from taking the ratio of the Lyβ and Heβ emissivity surfaces. Working one column, or core slice, at a time, the experimental emis-

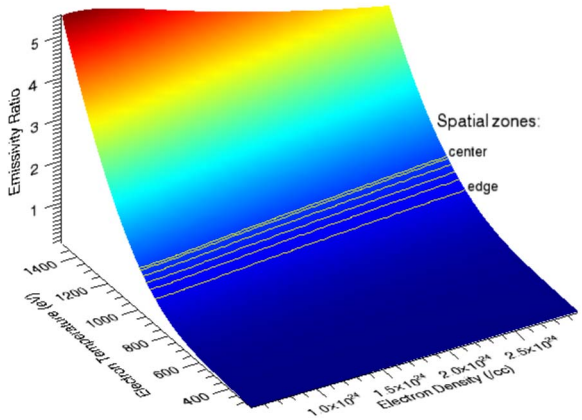

FIG. 3. (Color online) Contours representing the experimental emissivity ratio values in each spatial zone, mapped onto the theoretical emissivity surface. The experimental data is from the six spatial zones of the central core slice.

sivity ratio for each spatial zone is contour plotted onto the theoretical emissivity ratio surface. These contours can also be seen in Fig. 3, and clearly display the density insensitivity of the Lyβ/Heβ emissivity ratio. In other words, across a wide range in density, the temperature changes very little. Effectively, the equation relating experimental and theoretical emissivity ratios is solved. The temperature profile for a particular column is calculated by averaging the temperatures along the individual contours in a reasonable yet broad density range. The temperature spread is then used to determine the uncertainty in the temperature profile calculation.

Figure 4 displays an example of a 1D temperature profile from the central column, as well as a map of the temperature throughout the six central core slices. The maps shown in this paper were reconstructed by individually calculating the profile for each column and then reflecting each profile about its local gummy-worm axis of symmetry. Viewed from above, these are spatial maps which relate to the spatial coordinates seen in the images of Fig. 1(b). The temperature map of Fig. 4 shows several notable characteristics. Generally, the temperatures slope downward at the edges of the core (the top and bottom of the map). The temperature appears to be higher toward the left side of the image, which could be due to experimental deviations from spherical symmetry that resulted in the formation of an asymmetric hot spot. The temperatures generated with this analysis are consistent in both trend and absolute value with the profiles provided by 1D hydro simulations.

Using the information from the temperature profile analysis, the density profiles can be extracted by solving either the Lyβ or Heβ emissivity equations,

$$\epsilon_{Ly\beta}^{exp} = k\epsilon_{Ly\beta}^{theory}(T_e, N_e), \tag{2}$$

$$\epsilon_{He\beta}^{exp} = k\epsilon_{He\beta}^{theory}(T_e, N_e). \tag{3}$$

In these equations, experimental and theoretical emissivities are linked by a proportionality constant, k. The only unknowns are k and the density, N_e. Given a particular value for

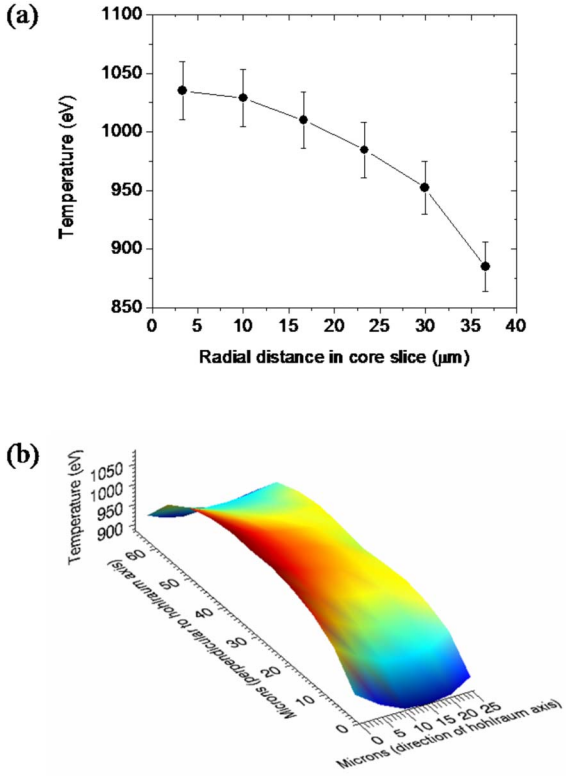

FIG. 4. (Color online) (a) Temperature profile for the central core slice. The uncertainty bars represent the weak density sensitivity in each spatial zone. (b) Quasi-3D representation of the temperature map, plotted as a function of distance in microns, for the central six columns of the images.

k, the solution is unique. Changing the value of k retains the shape of the profile but changes the absolute densities. To solve this problem, an iterative technique has been developed to accurately identify the absolute density values. Trial profiles are recalculated for different central density values, and following the calculation of each trial profile, an emissivity-weighted average is performed to represent a single spatially averaged density value. This emissivity-weighted average is then compared to the independently determined results of the uniform model analysis, which acts as a constraint. In this particular case, the uniform model analysis used the space-integrated line spectrum including the Lyβ and Heβ features to determine the spatially averaged density conditions throughout the core. The trial profile with the closest match between the emissivity-weighted average and the uniform model result is then considered to be the density profile solution.

The uncertainties are determined by recalculating the density profiles using the high and low value from the temperature spread in each spatial zone. The uncertainties are quite small due to the fact that variations in the temperature values (as depicted in the uncertainty spread of Fig. 4) produce very similar density values. In other words, the calculation of the density profiles is relatively insensitive to the temperature.

Figure 5 shows the central core slice density profiles based on both Lyβ and Heβ, and the full density map of the central six columns of the image, based on the Lyβ. The

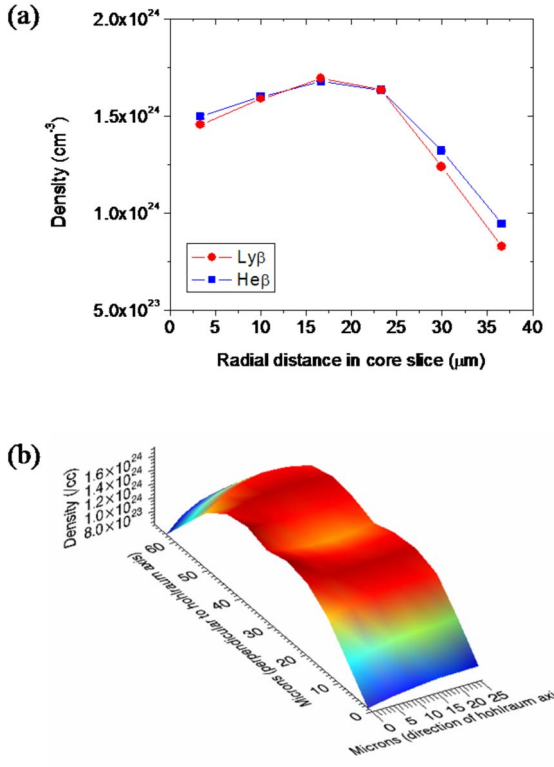

FIG. 5. (Color online) (a) Density profiles for the central core slice, based on the Lyβ and Heβ emissivity equations. (b) Quasi-3D representation of the density map based on the Lyβ, plotted as a function of distance in microns, for the central six columns of the images.

density profiles consistently demonstrate the general trend of downward sloping profiles with a central dip in the middle. It is noted that the spatial profiles based on the Lyβ and Heβ line features compare very well.

V. INTENSITY ANALYSIS

An alternative technique to extract the core density profiles has been developed. The experimental data available in this work consists of narrow-band images representing intensity on the image plane. The idea for the intensity analysis is to take advantage of the principles of image formation in order to provide a theoretical framework for setting up discrete radiation transport equations. The major benefit of the intensity analysis is that it facilitates the inclusion of opacity effects associated with the Lyβ, Heβ, and Lyα lines, specifically by studying the impact the opacity has on the density profiles.

The emissivity analysis, which was performed in the optically thin approximation, relied on Abel inversions of the spatial intensity profiles. The intensity analysis, however, does not require Abel inversion to extract density. It can be performed in the optically thin approximation and the results can be compared to the emissivity analysis results, which helps test the accuracy of the Abel inversion. When the intensity analysis is performed including the effects of opacity,

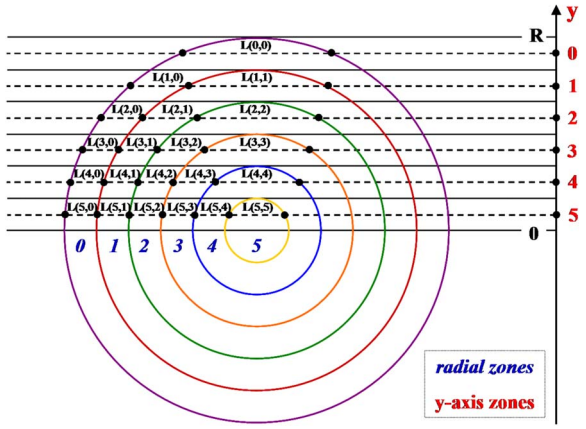

FIG. 6. (Color online) Image formation and setup for discrete transport equations.

the results demonstrate that even for lines such as the Lyβ and Heβ, which have mild optical depths, there are significant changes to the density spatial profiles.

In order to test these methods, synthetic data based on 1D hydro simulations were used. The results of these tests were encouraging, and demonstrated clearly that in the case of synthetic data, the known temperature and density profiles can be fully recovered for both the emissivity and intensity analyses [29].

The discrete radiation transport equations that model image intensity profiles were developed with the aid of Fig. 6. The y-axis zones represent intensity on the image plane, which is available in the experimental data. R represents the core slice size, which is broken into six equally spaced intervals. The zones on the image plane and in the object space share the same grid. The chord lengths, $L(i,j)$, are calculated using simple geometric considerations.

The theoretical intensity equations themselves are built by including terms which represent self-emission and attenuation. The analysis starts with the outer zone of the core and moves inward, since information from the previous zones in the calculation (zones further toward the edge of the core) is necessary. The equations become significantly more complicated as radiation is transported through multiple zones. As an example, the intensity equation of the first outer zone is given here:

$$I_\nu(0) = k' \frac{\epsilon_\nu(0)}{\kappa_\nu(0)} (1 - e^{-\kappa_\nu(0) L(0,0)}) \tag{4}$$

The equations for other spatial zones follow the same format, but include a number of additional self-emission and attenuation terms [30]. Effectively, in the analysis, the left-hand side of each equation represents the experimental intensity value for that particular spatial zone, while the right-hand side represents the self-emission and attenuation terms multiplied by a proportionality constant k'. This factor k' effectively relates experimental to theoretical intensity values. It is based on the k used in the emissivity equations, which relates experimental and theoretical emissivities, as well as on the magnification of the data. The intensity equations are

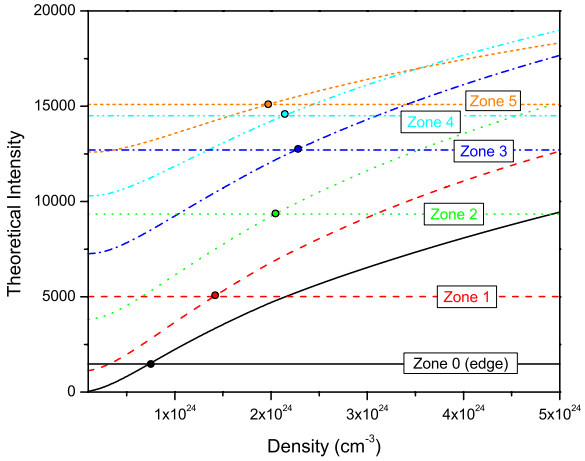

FIG. 7. (Color online) Plot showing the uniqueness of solution using the intensity analysis. The six spatial zones are based on the central core slice. Intersections between the horizontal lines (the experimental intensity values) and the curves (the theoretical intensities) give the density for each spatial zone.

dependent on the narrow-band emissivity, ϵ_ν, and opacity, κ_ν, in each spatial zone, which are functions of temperature and density, and on the chord lengths $L(i,j)$. The opacities used are actually emissivity-weighted opacities, in order to properly account for the contributions throughout the entire narrow-band energy range.

In order to build the density profiles, the intensity equations are solved zone-by-zone (moving inward) for the density assuming the temperature given by the emissivity ratio technique described in Sec. IV. This is why the intensity analysis is recognized as a semi-independent analytical technique, since it still relies on the temperature extracted from the emissivity analysis. The results of the intensity analysis are determined from zone-specific plots of the theoretical intensity [the right-hand sides of the intensity equations which follow the form of Eq. (4)] as a function of density. Drawing a horizontal line representing the experimental intensity for that zone results in intersecting the function once. This intersection point directly gives the density value. Figure 7 demonstrates this technique, and also clearly shows the uniqueness of the solution in the density range being investigated.

The first step is to calculate the density profiles in the optically thin approximation. In this case, only the self-emission terms of the intensity equations are used, and the optical depths $\tau=\kappa L$ are set equal to zero. The next step is to do the full calculation including opacity effects and using equations of the form described in Eq. (4).

Figure 8 shows a comparison of the Lyβ-based density profiles extracted from the three analyses: (i) the intrinsically optically thin emissivity analysis, (ii) the optically thin intensity analysis, and (iii) the intensity analysis including opacity effects. These results come from the Lyβ emissivity and intensity equations, and represent the central core slice of the images in Fig. 1. Using the Heβ equations produces very similar results. Also shown in Fig. 8 is the density map including opacity effects and based on the Lyβ. It is clear that

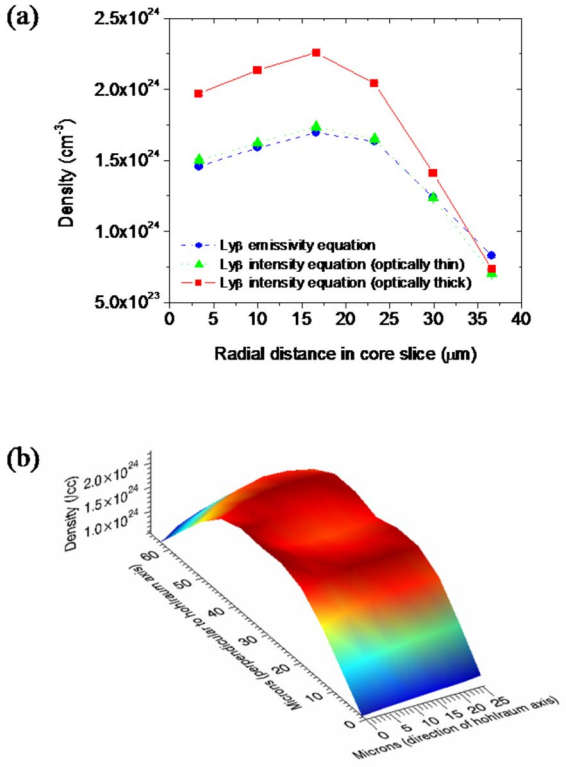

FIG. 8. (Color online) (a) A comparison of density profiles based on the Lyβ. Results are from the emissivity analysis, the intensity analysis using an optically thin approximation, and the intensity analysis including opacity effects. (b) Quasi-3D representation of the density map based on the Lyβ including opacity effects, plotted as a function of distance in microns, for the central six columns of the images.

even for a line as optically thin as the Lyβ, there is a noticeable opacity effect, particularly in the inner zones which have a greater optical depth.

A caveat here is that the density profiles resulting from the intensity analysis are not renormalized in any way. Recall that for the emissivity analysis, the emissivity-weighted average of the profiles was compared to the uniform model analysis, which acted as a constraint. Though the profile shape does not change, the absolute values do. In the intensity analysis results shown in Fig. 8, no such constraint has been implemented, so that it is easier to visualize the opacity effect in relation to the emissivity analysis results zone by zone.

VI. COMPARISON OF ANALYTICAL TECHNIQUES AND GENETIC ALGORITHM SEARCH METHOD

A method which reconstructs the temperature and density profiles using a genetic algorithm (GA) search engine was previously developed in an application to x-ray spectroscopy [14,18]. This spectroscopic technique was further expanded to include three objectives [17] and a parallel genetic algorithm implementation.

The method is based on a multicriteria GA search for the temperature and density profiles that yield the best simulta-

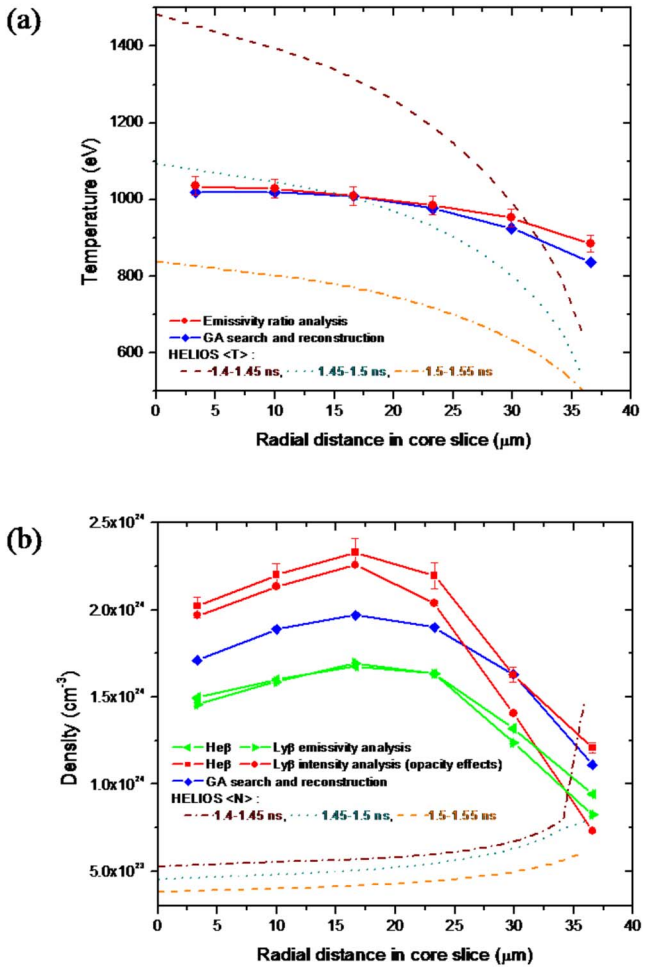

FIG. 9. (Color online) Comparison of emissivity and intensity analyses results, multi-objective search and reconstruction results, and HELIOS-CR 1D hydro simulations for (a) temperature and (b) density spatial profiles. Results are based on the central core slice of the images.

neous fits to an x-ray line spectrum and a collection of narrow-band emissivity profiles. Physically, the x-ray spectrum is one objective that provides information on spatially averaged conditions in the core. The other objectives are the Lyβ and Heβ emissivity profiles extracted from the narrow-band images, which yield a spatially resolved level of detail.

Since this method is completely independent of the emissivity and intensity analyses discussed in the previous two sections, it is useful to compare the spatial profiles. Figure 9 displays the temperature and density profiles resulting from the emissivity analysis, the intensity analysis, and the genetic algorithm-driven multi-objective search and reconstruction technique. The HELIOS-CR 1D hydrodynamics code [31,32] was run for the experimental case of interest, and the resulting temperature and density profiles are shown for comparison. These profiles have been post-processed to provide emissivity-weighted time averages over the duration represented in the data (50 ps in this case). The three traces in each plot represent three neighboring snapshots in time, since the timing between the hydro simulation and the experiment is not absolute.

The temperature profiles extracted from the two independent data analyses compare quite well. The time-averaged HELIOS-CR simulations show consistently steeper temperature profiles than are seen with the data analyses. The density profiles from the GA analysis fall between the intensity analysis results including opacity effects and the emissivity analysis results. This is due to the fact that the physics model used in the GA search technique uses some opacity information in the fitting of the spectrum. In contrast, the intensity analysis takes full account of the opacity effects, while the emissivity analysis neglects the opacity effects. Comparisons with the time-averaged HELIOS-CR density profiles are quite interesting, since the hydro consistently gives lower and very flat densities. One issue to note is the fact that these clean hydro simulations by definition do not include any mixing effects. However, mixing intrinsically affects the data, particularly toward the edges of the core. An investigation into this discrepancy is ongoing.

VII. MIXING INVESTIGATION BASED ON SPECTROSCOPIC DATA ANALYSIS

The inclusion of the additional Lyα data brings more information into the analysis. The ultimate goal is to extract realistic densities and spatial mixing profiles directly from the experimental data, using no prior assumptions. In order to include mixing in the analysis, equations of the form of Eqs. (2)–(4) are modified to include a mixing coefficient γ, which represents the local ratio of the atom number densities of plastic from the shell and deuterium from the fuel. It can be shown [30] that for the fill pressures and other attributes of the experiments described here, the intensity and emissivity equations become

$$I^{exp}_{Ly\alpha}(0) = k' \frac{\epsilon^{theo}_{Ly\alpha}(0)}{\kappa^{theo}_{Ly\alpha}(0)} \left[1 - e^{-\frac{1}{(1+7\gamma(0))}\kappa^{theo}_{Ly\alpha}(0)L(0,0)}\right], \quad (5)$$

$$\epsilon^{exp}_{Ly\beta \text{ or } He\beta}(0) = \frac{k}{(1+7\gamma(0))} \epsilon^{theo}_{Ly\beta \text{ or } He\beta}(0). \quad (6)$$

This is an example for the outer (simplest) zone, and the idea of multiplying the theoretical emissivities and opacities by a factor of $\frac{1}{1+7\gamma}$ carries over to all other zones. Recall that the emissivities and opacities are functions of temperature and density. Essentially, the only two unknowns in this system of two equations are the density N_e and the mixing coefficient γ. Note that the intensity from Eq. (5) is based on the Lyα, while the emissivity from Eq. (6) can be based on either the Lyβ or the Heβ. The density is calculated first by rearrangement of the equations and substitution. The resulting density is used to solve for the mixing coefficient, γ.

Due to opacity effects of the Lyα, the analysis breaks down after the outer two spatial zones. Therefore, the densities based on the Lyα as well as the mixing coefficients are only calculated for the two outermost zones. Very little change is seen when comparing the Lyα-based density profiles with and without the mixing effect.

Figure 10 presents the mixing coefficients extracted for the outer two zones of the three central columns of the im-

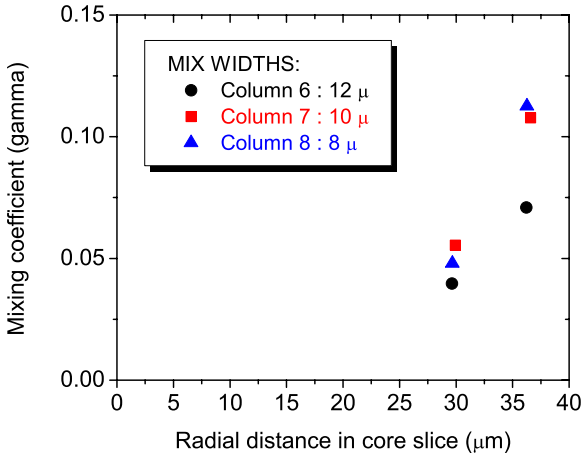

FIG. 10. (Color online) Mixing profiles calculated for the outer two spatial zones for three central columns of the images. Mix width estimations for each column are indicated.

ages in Fig. 1. A consistent trend is noticeable. According to this data-driven mixing analysis, the amount of mixing in these columns is at a maximum in the outer zone. The mixing coefficient γ is in the 5 to 12 percent range. It is possible to make a rough approximation of the mix width, which is defined as the radial size of the region that contains material from both the shell and the core. This can be done by calculating the scale length of the two points in the mixing profile. The rate of change of the γ function with respect to the distance axis, or the mix width h, can be defined with the following formula:

$$h = \frac{\gamma}{\left|\frac{d\gamma}{dx}\right|}. \tag{7}$$

The mix width estimates based on this scale length approximation are shown in Fig. 10 for the three mixing profiles. The average mix width for the three columns is 10 ± 2 microns.

Two independent theoretical mix models, Youngs' and Haan's model, have been implemented and described elsewhere [33]. Youngs' model [34], which calculates an effective lower-bound mix width, predicts values of 1.3–1.7 microns during the time corresponding to the data recording, while Haan's saturation model [35], which calculates a mix width by estimating the growth of multimode perturbations on the fuel-shell interface, predicts values of 3.8–4.0 microns.

We point out that these theoretical mix models calculate the size of the mix layer due to Rayleigh-Taylor growth only, and are probably underpredicting the mix widths. The accuracy of these mix models cannot as yet be tested by the data analysis techniques discussed here until a pattern has been established by forthcoming experiments which will attempt to constrain the problem.

VIII. CONCLUSIONS

The primary goal of this work has been to advance the spectroscopic analysis of ICF implosion cores by investigating different analysis methods and applying them to the extraction of spatial profiles of temperature and density. In addition, it has also been possible to extract quantitative information on fuel-shell mixing directly from these spectroscopic data analyses.

Two different spectroscopic techniques were developed to extract spatial profiles from narrow-band image and line spectrum data. Both methods permit a clear demonstration of the uniqueness of the solution. Temperature profiles are extracted first by exploiting the strong dependence of the Lyβ/Heβ emissivity ratio on the temperature. Density profiles are then calculated in two ways that yield distinct results. Using an emissivity analysis, the Lyβ and Heβ emissivity equations are solved separately to extract density profiles in the optically thin approximation. Utilizing an intensity analysis, which models the transport of radiation through the core, involves the solution of a set of nonlinear discrete transport equations. The intensity analysis can be performed either in the optically thin approximation, in which case the results compare well to those of the emissivity analysis, or including the effects of opacity, in which case a noticeable change in the spatial profile is seen for zones with higher optical depths. However, we emphasize that opacity effects on the temperature spatial profiles have not been investigated with these methods.

The utilization of additional spectroscopic data, e.g. in the form of the optically thick Lyα line, opens possibilities to study the spatial extent and level of mixing. In effect, using three pieces of data (the Lyβ, Heβ, and Lyα images), three unknowns (the temperature, density, and mixing coefficient) can be extracted. As discussed in this paper, information regarding the level of mix has been directly extracted from a data analysis using only spectroscopic arguments.

ACKNOWLEDGMENTS

We wish to acknowledge the support of DOE-NLUF Grants Nos. DE-FG52-2005NA26012 and DE-FG03-03SF22696 and LLNL.

[1] R. Mancini, C. Hooper, N. Delamater, A. Hauer, C. Keane, B. Hammel, and J. Nash, Rev. Sci. Instrum. **63**, 5119 (1992).
[2] H. Griem, Phys. Fluids B **4**, 2346 (1992).
[3] B. A. Hammel, C. J. Keane, M. D. Cable, D. R. Kania, J. D. Kilkenny, R. W. Lee, and R. Pasha, Phys. Rev. Lett. **70**, 1263 (1993).
[4] D. Haynes, C. Hooper, R. Mancini, D. Bradley, J. Delettrez, R. Epstein, and P. Jaanimagi, Rev. Sci. Instrum. **66**, 755 (1995).
[5] D. A. Haynes, D. T. Garber, C. F. Hooper, R. C. Mancini, Y. T. Lee, D. K. Bradley, J. Delettrez, R. Epstein, and P. A. Jaan-

imagi, Phys. Rev. E **53**, 1042 (1996).
[6] N. Woolsey, A. Asfaw, B. Hammel, C. Keane, C. Back, A. Calisti, C. Mosse, R. Stamm, B. Talin, J. Wark, R. W. Lee, and L. Klein, Phys. Rev. E **53**, 6396 (1996).
[7] N. Woolsey *et al.*, J. Quant. Spectrosc. Radiat. Transf. **58**, 975 (1997).
[8] N. Woolsey, B. Hammel, C. Keane, C. Back, J. Moreno, J. Nash, A. Calisti, C. Mosse, R. Stamm, B. Talin, A. Asfaw, L. S. Klein, and R. W. Lee, Phys. Rev. E **57**, 4650 (1998).
[9] S. Regan *et al.*, Phys. Plasmas **9**, 1357 (2002).
[10] H. Griem, *Principles of Plasma Spectroscopy* (Cambridge University Press, United Kingdom, 1996).
[11] B. Yaakobi, F. J. Marshall, and R. Epstein, Phys. Rev. E **54**, 5848 (1996).
[12] R. Lee, J. Quant. Spectrosc. Radiat. Transf. **27**, 87 (1982).
[13] I. Golovkin and R. Mancini, J. Quant. Spectrosc. Radiat. Transf. **65**, 273 (2000).
[14] I. Golovkin, R. Mancini, S. Louis, R. Lee, and L. Klein, J. Quant. Spectrosc. Radiat. Transf. **75**, 625 (2002).
[15] Y. Ochi *et al.*, Rev. Sci. Instrum. **74**, 1683 (2003).
[16] J. Koch, T. Barbee, N. Izumi, R. Tommasini, R. Mancini, L. Welser, and F. Marshall, Rev. Sci. Instrum. **76**, 073708 (2005).
[17] L. Welser *et al.*, J. Quant. Spectrosc. Radiat. Transf. **99**, 649 (2006).
[18] I. Golovkin, R. Mancini, S. Louis, Y. Ochi, K. Fujita, H. Nishimura, H. Shiraga, N. Miyanaga, H. Azechi, R. Butzbach, I. Uschmann, E. Forster, J. Delettrez, J. Koch, R. W. Lee, and L. Klein, Phys. Rev. Lett. **88**, 045002 (2002).
[19] S. Regan *et al.*, Phys. Rev. Lett. **89**, 085003 (2002).
[20] S. Regan *et al.*, Phys. Rev. Lett. **92**, 185002 (2004).
[21] C. Li *et al.*, Phys. Rev. Lett. **89**, 165002 (2002).
[22] B. Yaakobi, F. Marshall, D. Bradley, J. Delettrez, R. Craxton, and R. Epstein, Phys. Plasmas **4**, 3021 (1997).
[23] B. Yaakobi, F. Marshall, and D. Bradley, Appl. Opt. **37**, 8074 (1998).
[24] L. Welser, R. Mancini, J. Koch, H. Dalhed, R. Lee, I. Golovkin, F. Marshall, J. Delettrez, and L. Klein, Rev. Sci. Instrum. **74**, 1951 (2003).
[25] L. Welser *et al.*, J. Quant. Spectrosc. Radiat. Transf. **81**, 487 (2003).
[26] J. Koch *et al.*, AIP Conf. Proc. **730**, 53 (2005).
[27] K. Bockasten, J. Opt. Soc. Am. **51**, 943 (1961).
[28] C. Keane, B. Hammel, D. Kania, J. Kilkenny, R. Lee, A. Osterheld, L. Suter, R. Mancini, C. Hooper, and N. Delamater, Phys. Fluids B **5**, 3328 (1993).
[29] L. Welser-Sherrill *et al.*, High energy density physics **3**, 287 (2007).
[30] L. Welser, Ph.D. thesis, University of Nevada, 2006 (unpublished).
[31] J. MacFarlane, I. Golovkin, and P. Woodruff, J. Quant. Spectrosc. Radiat. Transf. **99**, 381 (2005).
[32] J. J. MacFarlane, I. E. Golovkin, R. C. Mancini, L. A. Welser, J. E. Bailey, J. A. Koch, T. A. Mehlhorn, G. A. Rochau, P. Wang, and P. Woodruff, Phys. Rev. E **72**, 066403 (2005).
[33] L. Welser-Sherrill *et al.*, Phys. Plasmas **14**, 072705 (2007).
[34] D. Youngs, Physica D **12**, 32 (1984).
[35] S. W. Haan, Phys. Rev. A **39**, 5812 (1989).